Chemical Microsystem Based on Vertical Integration of Sensor Array and CMOS Circuit

Final Report: Project Activities

O. Brand, School of Electrical and Computer Engineering
B. Mizaikoff, School of Chemistry and Biochemistry

Georgia Institute of Technology, Atlanta, GA 30332

Contents

I. Mass-Sensitive Resonant Microstructure

The aim of this part of the project is the fabrication and characterization of the micromachined resonant structure. A disk-shape microstructure capable of sustaining oscillations in a gas environment has been fabricated. The device operates in a rotational in-plane mode with typical resonance frequencies ranging between 300 kHz to 1000 kHz.

I.1 Mass-Sensing Principle

A resonant microstructure covered with a sensitive layer can be used as mass-sensitive sensor. Resonant microsensors operate as a harmonic oscillator with damping. This operation can be described by the force-deflection relation in the frequency domain

$$\frac{X(\omega)}{F(\omega)} = \frac{1}{-M\omega^2 + jB\omega + K} \qquad \textbf{(I.1)}$$

where M is the effective mass, K is the spring constant, and B is the damping coefficient. From Eqn I.1, the resonance frequency f_0 of the structure can be extracted as

$$f_0 = \frac{1}{2\pi}\sqrt{\frac{K}{M}} \qquad \textbf{(I.2)}$$

Consequently, the relative resonance frequency change of the sensor is given by

$$\frac{\Delta f}{f_0} = -\frac{1}{2}\frac{\Delta m}{M} + \frac{1}{2}\frac{\Delta k}{K} \qquad \textbf{(I.3)}$$

where Δf is the frequency change, Δm is the mass variation, and Δk is the spring constant variation of the microstructure. Therefore, if the spring constant variation can be neglected, a shift in the resonance frequency of the structure only depends on the absorption/desorption of an analyte in the sensitive layer which increases/decreases the oscillating mass of the microstructure.

The resolution of a mass-sensitive chemical sensor depends on the sensor sensitivity, i.e. the measured frequency change per change of analyte concentration (in units of Hz/ppm or Hz/(μg/L)) and the minimal detectable frequency change of the resonator. The minimal detectable frequency change of a resonant microstructure operated in a closed loop configuration is related to the short-term frequency stability of the resonance frequency, as measured by the Allan Variance. The frequency noise at the output of the resonator (Δf_{noise}) is expressed by

$$\Delta f_{noise} \approx \frac{f_0 \delta\phi}{2Q} \qquad \textbf{(I.4)}$$

where Q is the quality factor, and $\delta\phi$ is the feedback loop phase noise. Therefore, in order to improve the minimal detectable frequency change, the Q-factor of the resonant

structure should be increased. One way to increase the Q-factor is to reduce the air damping.

The sensor sensitivity S is a function of the sorption characteristics of the chosen sensitive film, expressed by the partition coefficient, and the mass-sensing capability of the transducer

$$S = \frac{df}{dc} = \frac{df}{d\rho_L} \cdot \frac{d\rho_L}{dc} = G \cdot S_A \qquad \textbf{(I.5)}$$

where c is the analyte concentration [µg/L], ρ_L is the density of sensitive layer [kg/m^3], G is the pure mechanical sensitivity of the resonator to a change in density of the sensitive layer [Hz/(kg/m^3)], and S_A [(kg/m^3)/(µg/L)] is the sensitivity related to the sorption characteristics of the sensitive coating. A prominent point accounted for in Eqn I.5 is that the density sensitivity G of a resonator is critical for chemical sensing, not the mass sensitivity. The mass sensitivity of a resonator can simply be improved by shrinking the resonator dimensions, i.e. its mass. However, the volume of the sensitive layer is reduced with the dimension of the resonator, which results in a reduced analyte uptake and, thus, no improvement in chemical sensitivity.

Consequently, in order to improve the sensor resolution, resonant microstructures should be designed with a high sensitivity and a high Q-factor while providing sufficient sensing area covered with the sensitive layer.

I.2 Fundamental Sensor Structure

Fig I.1a shows the SEM image of a fabricated disk resonator. Two semi-circular disks are attached to a central silicon anchor beam by support beams. In order to increase the Q-factor in air, the presented disk-shape microstructures vibrate in an in-plane mode (see Fig I.1b), thus shearing instead of compressing the surrounding media. This results in reduced air damping and improved Q-factors.

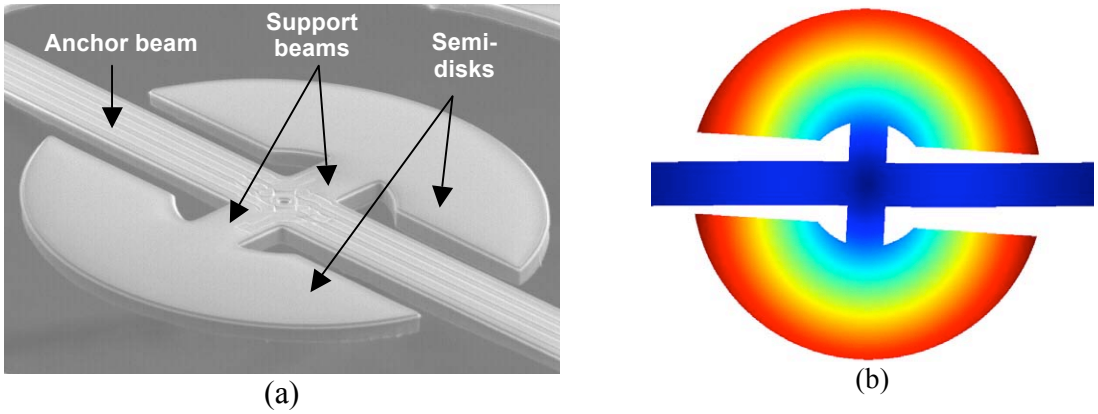

(a) (b)

Fig I.1: *a) SEM image of a disk resonator, b) Rotational in-plane mode of the disk resonator simulated with FEM software FEMLAB (the two semi-disks vibrate in an in-plane mode).*

The resonator structures must have proper excitation and sensing mechanisms that will sustain in-plane mode vibrations at the resonance frequency. An electrothermal excitation mechanism is implemented using an asymmetric arrangement of diffused heating resistors along the semi-disk support beams (see Fig I.2). Besides, silicon piezoresistors arranged in a Wheatstone bridge at the center of the anchor beam are used as the detection element (see Fig I.2), designed to be sensitive to in-plane rotational vibration modes, but not to out-of-plane modes. Both excitation and detection mechanisms are simple, effective, and only use resistive elements readily available in most microfabrication technologies.

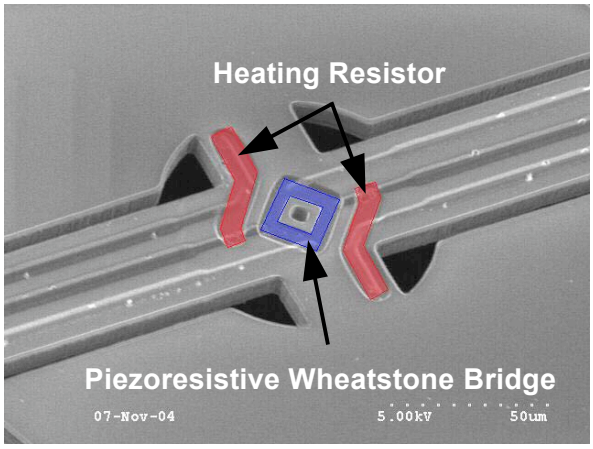

Fig I.2: *SEM image of center part of a disk resonator, where heating resistors and piezoresistive Wheatstone bridge are located.*

Fig I.3a shows the electrical connections to the heating resistors and the Wheatstone bridge. The excitation signals (see Fig I.3b) are applied to the terminals V_{EX1} and V_{EX2}, while the output signal of the Wheatstone bridge is read-out differentially from the terminals V_{S+} and V_{S-}.

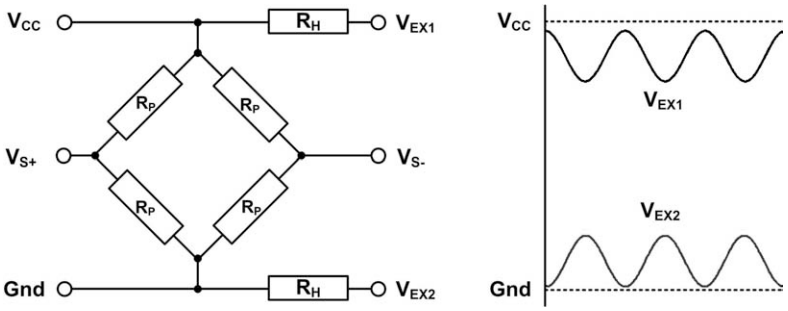

Fig I.3: *a) Electrical connections to the heating resistors and the Wheatstone bridge, b) Excitation signals applied to the terminals V_{EX1} and V_{EX2}.*

I.3 Additional Sensor Structures

Sensor Chip for Flip-Chip Bonding

The sensor chip with an array of disk-shape resonators was redesigned to enable the vertical integration with a CMOS circuitry chip by wafer/chip bonding. Fig I.4 shows an SEM image of a fabricated sensor chip, which includes two disk-shape resonators. The pads have been placed for proper flip-chip bonding. In addition, alignment marks have been included which will allow alignment of the CMOS and MEMS chips during flip-chip connection. Although the resonator structure has been modified, it has the same operation principle and similar performance compared to the previous sensor structure.

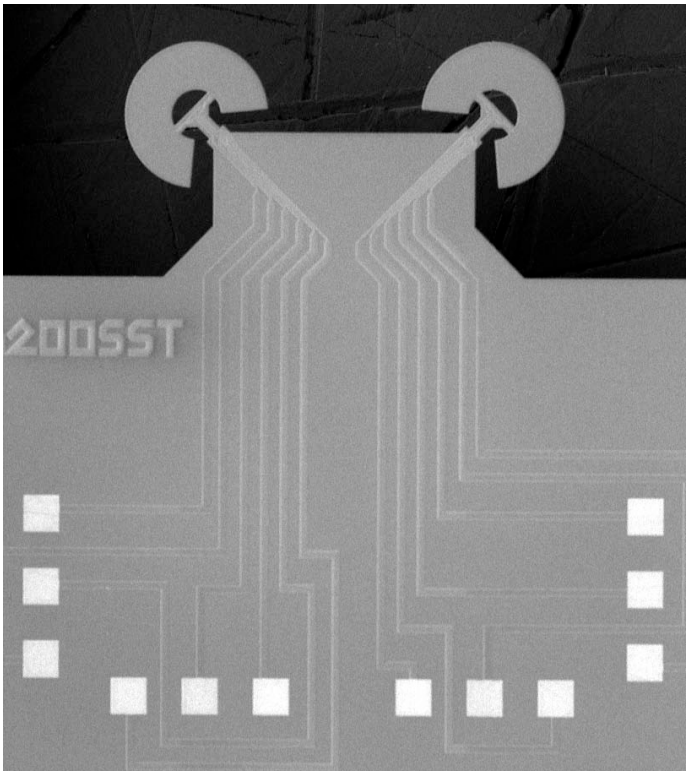

Fig I.4: *SEM image of a fabricated MEMS chip.*

Disk- and Annular-Type Microresonators

Based on the initial designs, two novel types of disk resonator geometries (see Fig. I.5) were designed and tested: the disk geometry involves two half-disks attached to a central main anchor, and has rotational in-plane resonant frequencies of 290–550 kHz; the annular geometry involves two half annuli with an inner radius of 100 μm attached to a central main anchor, and has resonant frequencies of 220–465 kHz.

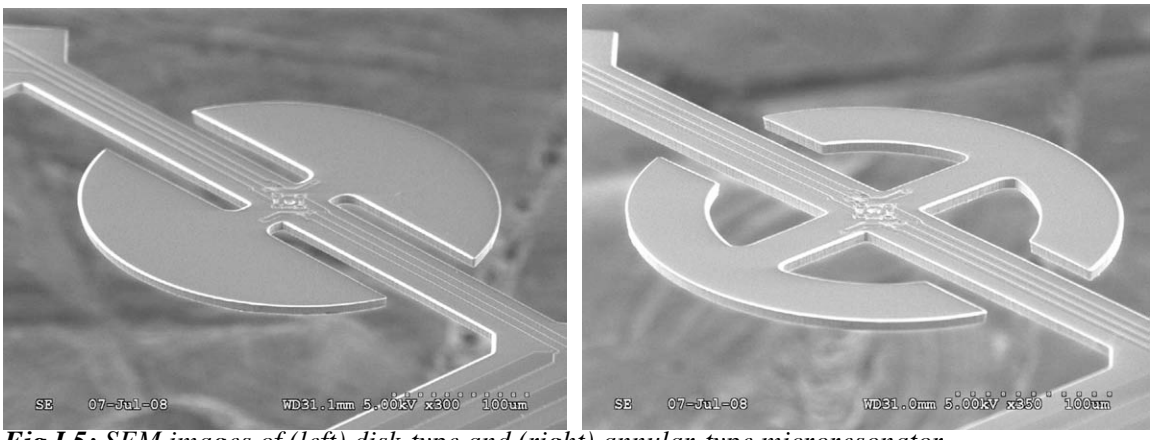

Fig I.5: *SEM images of (left) disk-type and (right) annular-type microresonator.*

I.4 Sensor Fabrication

The fabrication process of the disk resonators starts with a (100) silicon epi-wafer with a phosphorous-doped epitaxial layer on top of a p-substrate. The epi-layer thickness defines the final resonator thickness after anisotropic silicon etching with an electrochemical etch-stop technique.

First, a 1 μm silicon dioxide layer is grown thermally in a wet oxidation tube at 1050 °C. After patterning a silicon dioxide diffusion mask, p-type piezoresistors and heating resistors are diffused (see Fig I.6a). Pre-deposition diffusion was done with boron solid sources at 930 °C for 1 hr, giving 150 Ω/□ sheet resistance. Drive-in diffusion and thermal oxidation on top of the boron diffused areas were done at the same time in a thermal oxidation furnace. After etching contact openings with an ICP (Inductively Coupled Plasma) etcher, a 0.8 μm aluminum layer is sputtered and patterned by wet etching, followed by sintering in forming gas at 425°C for 40 minutes (see Fig I.6b). A low-stress PECVD (Plasma Enhanced Chemical Vapor Deposition) silicon oxide/nitride sandwich layer is deposited on the top of the wafer as an insulation layer and patterned to define areas that are etched away during the final structure release (see Fig I.6c). Next, a PECVD silicon nitride film is deposited and patterned on the back of the wafer to act as KOH etch mask. Finally, the microstructures are released by anisotropic silicon etching using a 6 molar KOH solution at 75 °C with an electrochemical etch-stop technique, followed by RIE (Reactive Ion Etching) from the top of the wafer using the PECVD oxide as an etch mask (see Fig I.6d).

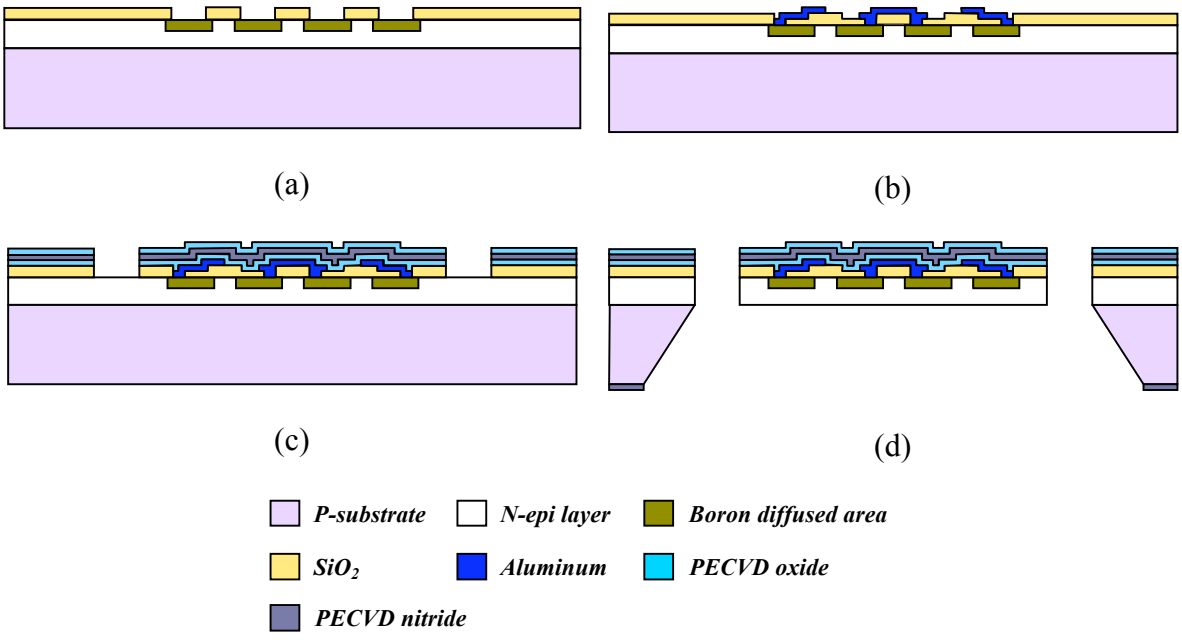

Fig I.6: *Fabrication process flow for disk resonator.*

II. Sensor Characterization

II.1 Open-Loop Characterization

In order to investigate the influence of the device dimensions on Q-factor and resonance frequency, an analytical model describing the resonant behavior of the disk resonator has been derived. This model forms a guide in choosing the dimensions of the resonant sensors which reduces the design and characterization time considerably. To check the validity of the analytical model and to see the effects of device dimensions on the resonator performance, microstructures with different dimensions have been fabricated and examined (see Fig II.1a). Fig II.1b shows the varied device dimensions. The device dimensions are chosen to have sufficiently large sensing area while maintaining a resonance frequency in the range of 350 - 1,000 kHz for simplified integration of on-chip microelectronics in the future. Table II.1 gives the chosen resonator dimensions.

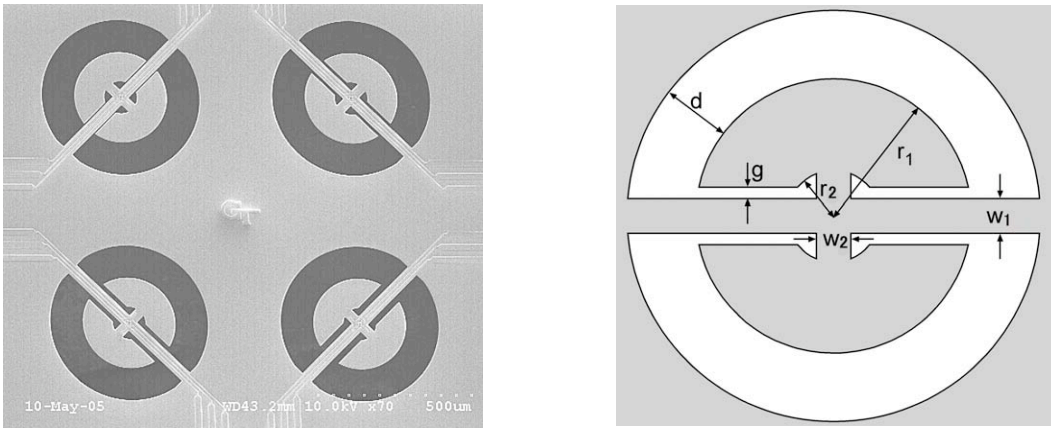

(a) (b)

Fig II.1: *a) SEM image of four disk resonators with different dimensions, b) Schematic of the disk resonator with notations of key structure dimensions,*

Dimensions (see Fig I.5b)	r_1 : 120, 140, 150 µm r_2 : 40, 50 µm g : 5, 10, 15, 20 µm d : 50, 100 µm t (thickness): 8± 2µm w_1 : 35, 40, 45 µm w_2 : 30, 40 µm
Resonance frequency	350 ~ 1,000 kHz

Table II.1 *Dimensions of the fabricated resonators.*

The fabricated resonant microstructures have been characterized in air. The amplitude transfer characteristics have been recorded using an Agilent 4395A network/spectrum analyzer. Fig II.2a shows the output signal of the piezoresistive Wheatstone bridge of a disk resonator with dimensions $r_1 = 120\ \mu m$, $r_2 = 50\ \mu m$, $g = 15\ \mu m$ and $d = 100\ \mu m$ in the

frequency range of 100 kHz to 1 MHz. Only the in-plane vibration mode of interest around 600 kHz is visible in the output spectrum. All low-frequency, out-of-plane resonant modes are efficiently suppressed by the chosen actuation and detection method which simplifies the operation of the resonators in an amplifying feedback loop.

Fig II.2b shows the amplitude and phase of the Wheatstone bridge output signal of the same resonator around the in-plane resonance frequency. A Q-factor of 5,823 has been extracted from the 3dB-bandwidth of the resonance.

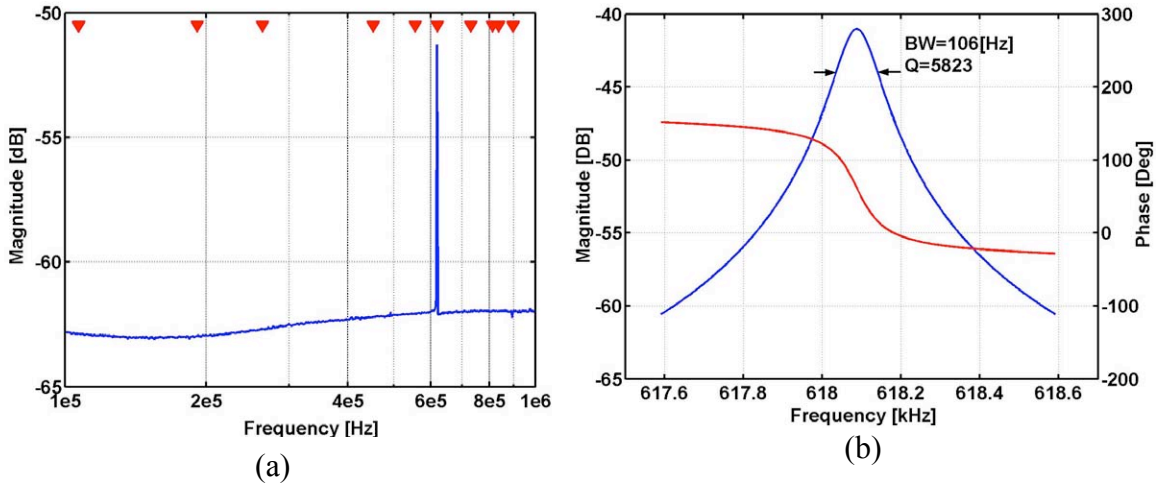

(a) (b)

Fig II.2: *a) Amplitude transfer characteristic of a disk resonator with r_1 = 120 µm, r_2 = 50 µm, g = 15 µm and d = 100 µm from 100 kHz to 1 MHz, b) Amplitude and phase plot of the piezoresistive Wheatstone bridge output signal around in-plane resonance frequency.*

Resonators with different dimensions and geometries have been tested in air to determine the Q-factor and resonance frequency, and compare experimental results with analytical estimations. Fig II.3 shows the measured resonance frequencies together with estimated resonance frequencies from the analytical model for various structure dimensions, demonstrating that the developed analytical model matches quite well with the experimental results. Fig II.4 gives the measured Q-factors of two resonators with different thicknesses (t=6μm and t=10μm) as a function of the gap g along with the estimated Q-factors obtained from the analytical model (dashed lines in the plot). Even though the measured Q-factors in Fig II.4 are generally lower than those obtained from the analytical solution (because the squeezed-film damping has not been considered in the analytical model), the derived damping model provides an upper limit for Q-factor and is sufficient for design optimization of the proposed rotational in-plane resonance mode microstructures.

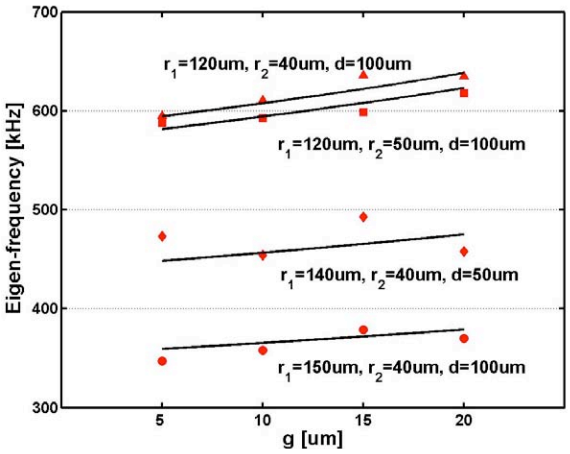

Fig II.3: *Resonance frequency of disk resonators with different dimensions r_1, r_2, d as a function of the gap size g; solid line: analytical solution, symbols: experimental results.*

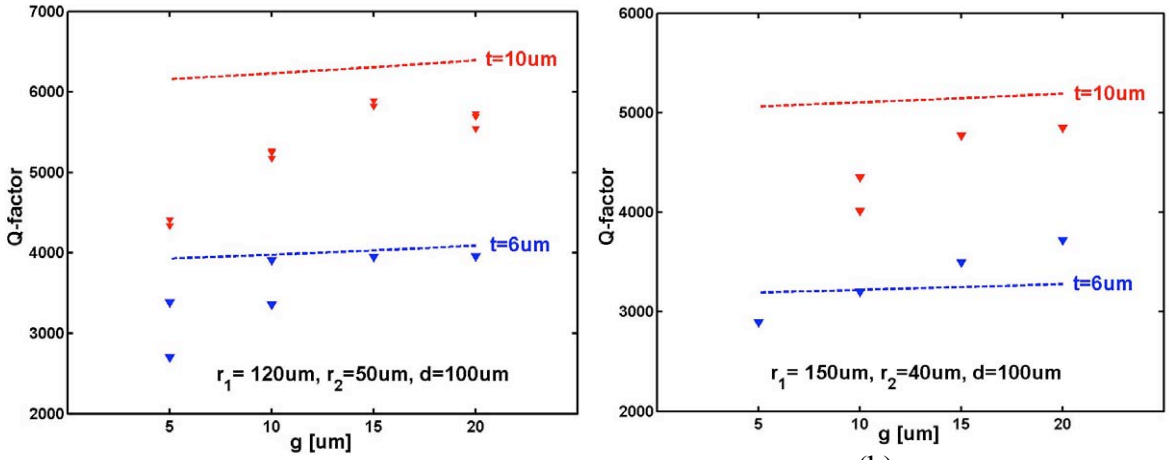

Fig II.4: *Q-factor of in-phase rotational mode as a function of the air gap g for two different resonator geometries [(a) r_1=120μm, r_2=50μm, d=100μm; (b) r_1=150μm, r_2=40μm, d=100μm] and two device thicknesses t = 6 and 10 μm; dashed lines: analytical solution; symbols: experimental results.*

II.2 Closed-Loop Characterization

This section of the project focuses on the closed loop operation of the disk resonators. A custom built printed circuit board (PCB) that uses off-chip components forms the off-chip feedback loop circuitry. In addition, an integrated version of the same amplifying loop, which is called on-chip feedback loop circuitry for the sake of clarity, was designed and fabricated. With this feedback loop, the resonators as frequency determining elements operate in self-oscillation. In order to determine the minimal detectable frequency change of the resonators, short-term frequency stability measurements have been performed. An important part of this section concentrates on a novel stiffness compensation scheme that removes the drift in the resonance frequency caused by stiffness changes.

As mass-sensitive chemical sensors, the fabricated resonators are operated as frequency-determining elements in a self-oscillating amplifying feedback loop, as shown in Fig II.5. The piezoresistive Wheatstone bridge signal (detection signal) is amplified and high-pass filtered to remove DC offset and flicker noise. Then, this signal is fed to a phase adjusting circuit (all-pass filter). The gain stage and the phase shifter are used to meet the Barkhausen condition which ensures the overall system acts as a positive feedback loop at the resonance frequency. The phase-tuned signal is then applied to a Schmitt-trigger circuit which acts as an amplitude limiter. While generating an amplitude-limited square wave, the Schmitt-trigger extracts the phase information of the signal. Thereafter, a DC bias voltage is added to the square wave signal and then applied to the heating resistors, thus closing the loop. With the capability of the implanted Wheatstone bridge of rejecting parasitically coupled signals in conjunction with a strong signal only at the chosen resonance frequency, stable operation of the resonators in an amplifying feedback loop is realized. The resonance frequency is measured with an Agilent 53131 frequency counter connected at the output of the Schmitt-trigger.

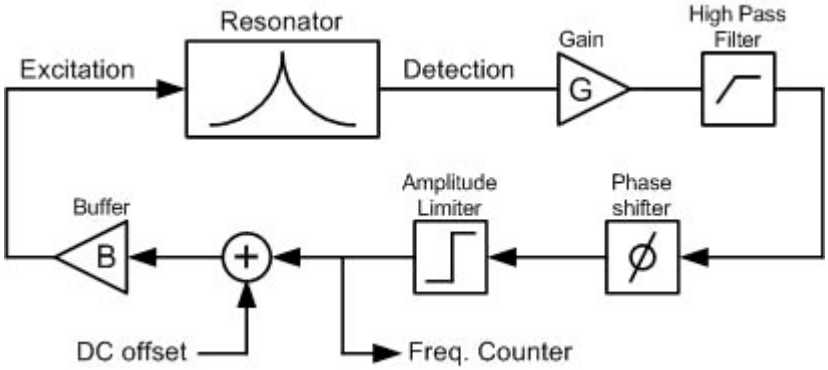

Fig II.5: *Schematic diagram of the off-chip feedback loop circuitry.*

The feedback loop is implemented on a PCB using off-chip components as seen in Fig II.6.

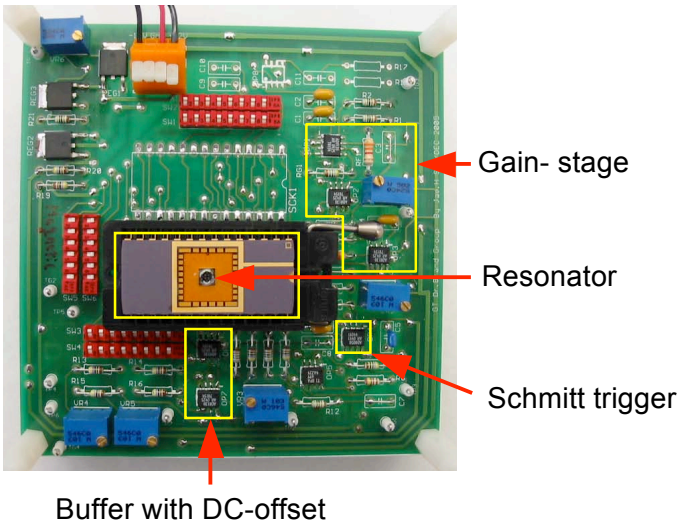

Fig II.6: *Off-Chip feedback loop circuit on a printed circuit board (PCB).*

In order to estimate the short-term frequency stability in air, which determines the frequency resolution of the resonator, the resonance frequency of the resonators is recorded using an Agilent 53131 frequency counter with a gate time of 1 sec (see Fig II.7). This measurement has been carried out using off-chip feedback circuitry.

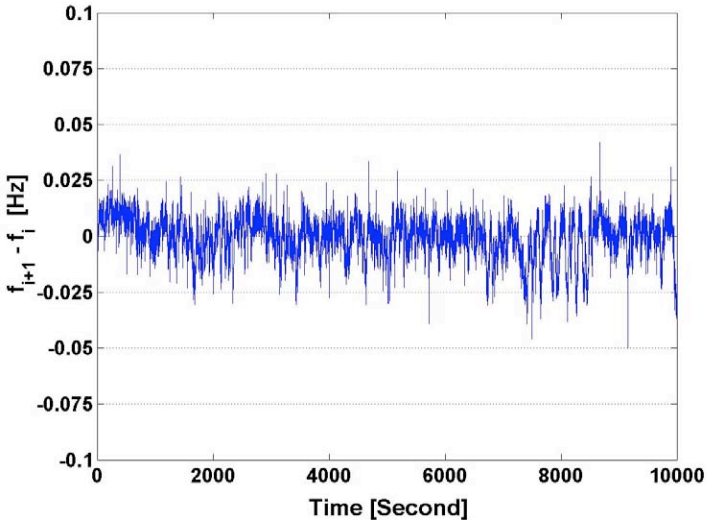

Fig II.7: *Recorded resonance frequency of the resonator with a gate time of 1 sec.*

The short-term frequency stability is estimated with the Allan variance method from the recorded frequency data. The Allan variance (σ) is defined as:

$$\sigma^2(\tau, m) = \frac{1}{2m}\sum_{n=1}^{m}(\gamma_{n+1} - \gamma_n)^2 \qquad \textbf{(II.1)}$$

with $\gamma_n = \frac{f_{n+1} - f_n}{f_n}$, the gate time τ, and number of measured data points m. Resonators with different dimensions have been used for measuring the short-term frequency stability in air. At least 10,000 data points (=10,000 seconds) are used to improve the reliability of the estimated Allan variance. The results are summarized in Table II.1. Frequency stabilities (estimated using Allan variances) as low as 1.07×10^{-8} have been measured in air up to now, i.e. a short-term frequency stability of 4.6 mHz for a resonator vibrating at 426 kHz.

Fig II.8 shows the Allan variances as a function of the gate time when the mass of the resonant sensor is constant. The increase in Allan variance with gate time, meaning a decreasing frequency stability, is caused by the drift of the resonance frequency. This drift is mainly due to the change in stiffness. Therefore, without compensating for the frequency change caused by a stiffness change, a high mass resolution cannot be achieved.

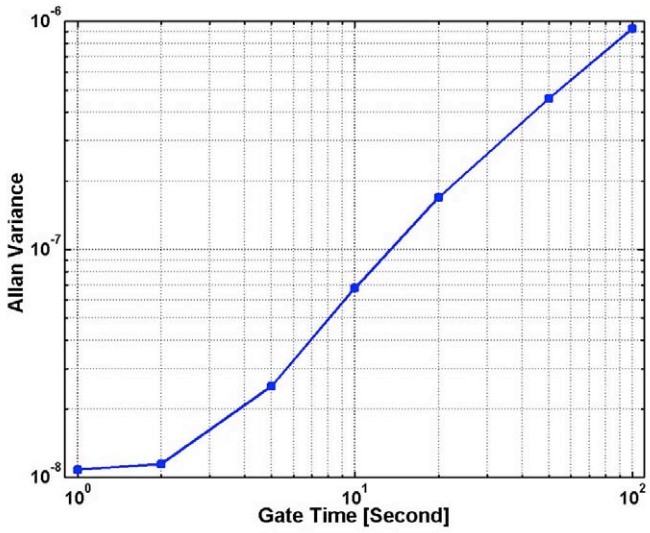

Fig II.8: *Allan variances of disk resonator as a function of gate time.*

Dimensions [μm]	Resonance Frequency	Allan Variance (σ / mHz)
r_1=140, r_2=50, w_1=35, w_2=30, g=15, l=480	411.0 kHz	1.50×10^{-8} / 6.2
r_1=140, r_2=40, w_1=35, w_2=30, g=15, l=480	421.5 kHz	2.62×10^{-8} / 11.0
r_1=140, r_2=40, w_1=35, w_2=30, g=20, l=480	426.2 kHz	1.07×10^{-8} / 4.6
r_1=140, r_2=50, w_1=45, w_2=40, g=10, l=380	644.3 kHz	1.21×10^{-8} / 7.8
r_1=120, r_2=50, w_1=40, w_2=40, g=10, l=340	886.5 kHz	2.14×10^{-8} / 19.0

Table II.1 *Summary of the measured short-term frequency stabilities in air with gate time of 1 second.*

III. Integrated Circuitry

An integrated version of the amplifying feedback loop circuit was designed and fabricated using the AMIS 0.5μm 3M2P CMOS process. Fig III.1 presents the architecture of the system consisting of sensor and CMOS chips, which can be hybrid or flip-chip connected to each other. The sensor chip consists of two microresonators. The CMOS chip includes two feedback loop circuits each of which will be connected to one of the microresonators on the sensor chip. Therefore, two resonators can be operated simultaneously allowing e.g. differential mode operation to minimize frequency Drift caused by temperature changes. The CMOS chip consists of an analog and a digital circuitry. In this first integrated design, digital circuitry is only responsible for multiplexing control signals to generate gain control signals. Also, on the chip are test

blocks including circuit blocks which form the analog circuitry. The inputs and outputs of the test blocks are connected to pads, thus allowing the testing of each block separately.

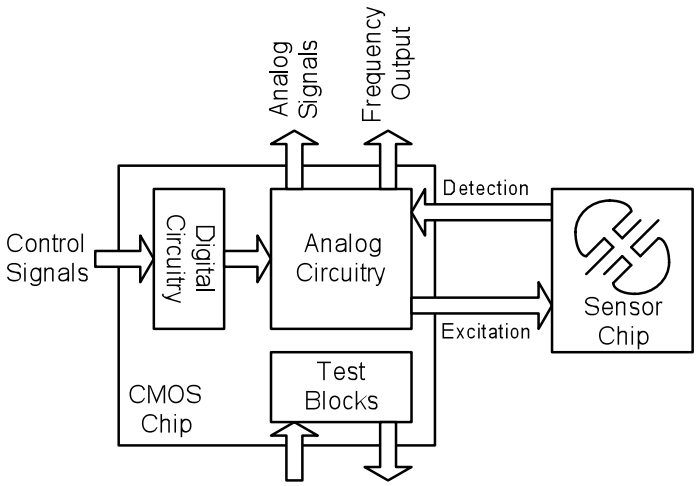

Fig III.1: *Architecture of designed CMOS chip.*

Fig. III.2 shows a micrograph of the fabricated 0.5 μm 3M2P CMOS ASIC including two feedback circuits allowing operation of two resonators at the same time. In the layout, the circuit blocks have been placed to allow flip-chip bonding of the CMOS chip with the sensor chip.

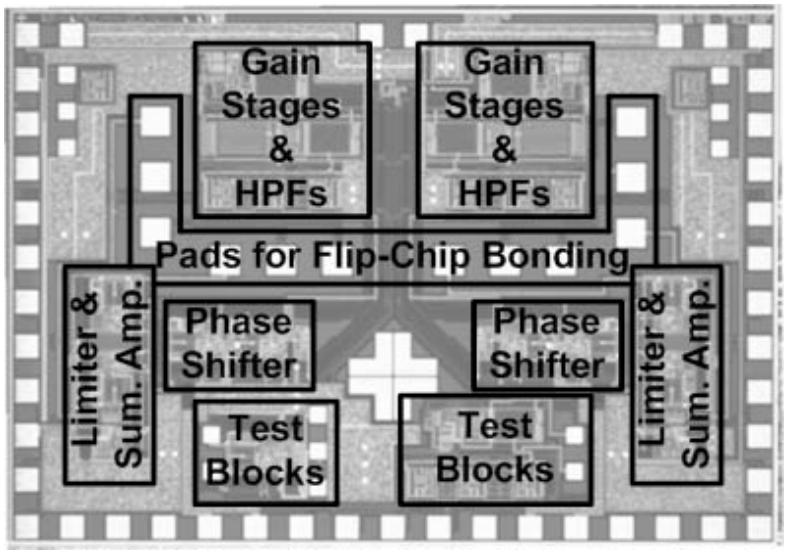

Fig III.2: *Micrograph of 0.5μm 3M2P CMOS ASIC including two feedback circuits.*

Fig. III.3 gives the schematic diagram of the feedback circuitry together with excitation and detection elements of the microresonator. The circuitry includes three gain stages to amplify the Wheatstone bridge signal (detection signal) from the sensor to meet unity gain condition and a phase shifter to meet the 0º phase condition. High-pass filters (HPFs) are implemented to remove DC-offset and flicker noise of the gain stages and the

Wheatstone bridge. An amplitude limiter is included to ensure stable oscillation while extracting the phase and frequency information from the signal.

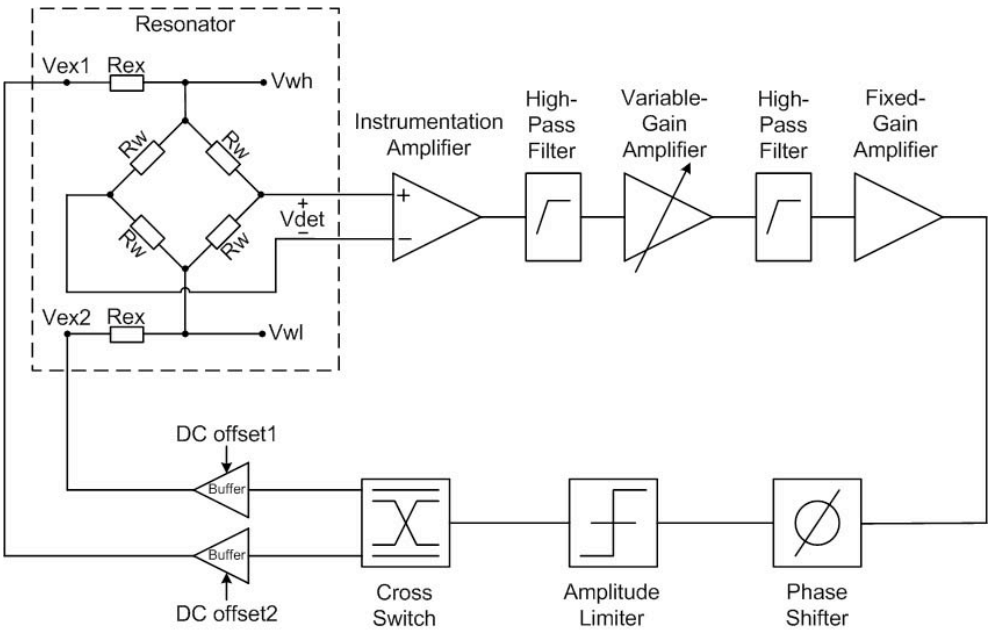

Fig III.3: *Schematic diagram of the on-chip feedback loop circuitry.*

To excite the resonator at its fundamental resonance frequency, summing amplifiers are used to add DC-offsets to the AC excitation signals. These summing amplifiers are implemented using class-AB opamps to be able to drive low-resistance excitation resistors (Rex in Fig. III.3). A cross-switch is also implemented to change the polarity of the excitation signals if needed. The supply voltage is ±2.5 V.

The following sections describe each block of the on-chip feedback circuitry in detail and also provide Cadence simulation results.

A. Gain Stages

The maximum signal attenuation by the resonators is 60 dB and varies in the range of 20 dB depending on resonator bias conditions, dimensions and fabrication-induced variations. Therefore, in total, the gain stages should provide at most 60 dB amplification with a tunable range of 20 dB without introducing additional phase shift up to a frequency of 800 kHz, which is the highest resonance frequency of the microresonators. Considering these requirements, three gain stages are implemented to ease the necessary gain-bandwidth product.

A three-opamp instrumentation amplifier (in-amp), a common way to interface Wheatstone bridges, is used as the first gain stage (see Fig. III.4). The gain of the in-amp is determined by the feedback resistors and given by

$$A_v = \left(1 + \frac{2R_2}{R_1}\right)\left(\frac{R_2}{R_1}\right) \qquad \textbf{(III.1)}$$

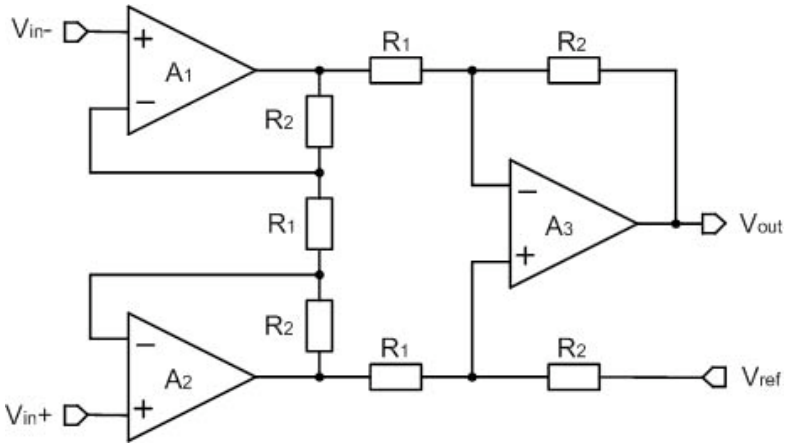

Fig III.4: *Schematic diagram of the three-opamp instrumentation amplifier used as the first gain stage.*

Fig. III.5 shows the measured amplitude response of the first gain stage with R_1 = 3kΩ and R_2 = 9kΩ. The gain is measured as 25.5 dB, high enough to reduce the effect of noise of consequent stages on the input while avoiding saturation of the amplifier because of offset of the Wheatstone bridge. The 3-dB cut-off frequency is extracted as 7 MHz, which is well above the sensor operation bandwidth. The phase shift introduced by this stage is -6° at 800 kHz.

The 20 dB tuning range is obtained with a variable-gain amplifier implemented as the second gain stage. This stage uses a non-inverting amplifier configuration with switched-resistors for gain adjustment. The measured closed-loop amplitude response (see Fig. III.6) shows gain variation between 5 dB and 25.5 dB. With the highest gain, the maximum phase shift at 800 kHz is measured as -5.8°.

The third gain stage is realized using a non-inverting amplifier with a gain of approximately 9 dB and a phase shift of -1.1° at 800 kHz. Overall, three gain stages provide amplification in the range between 39.5 dB and 59 dB. The maximum phase shift introduced by these gain stages is -12.9° at the highest sensor operation frequency of 800 kHz. Due to the high Q-factor of the microresonators and the phase shifter, this phase shift has little effect on the self-oscillation.

A two-stage Miller compensated opamp with a measured DC gain of 80 dB is used in the gain stages because of its lower noise performance compared to folded cascode opamps. The HPFs after the first and second gain stages are implemented using first-order RC-filters with a cut-off frequency of 4 kHz, which is much smaller than the lowest sensor frequency of 200 kHz. Thus, the HPFs do not affect the amplitude and phase responses of the feedback loop in the operation bandwidth of the sensor.

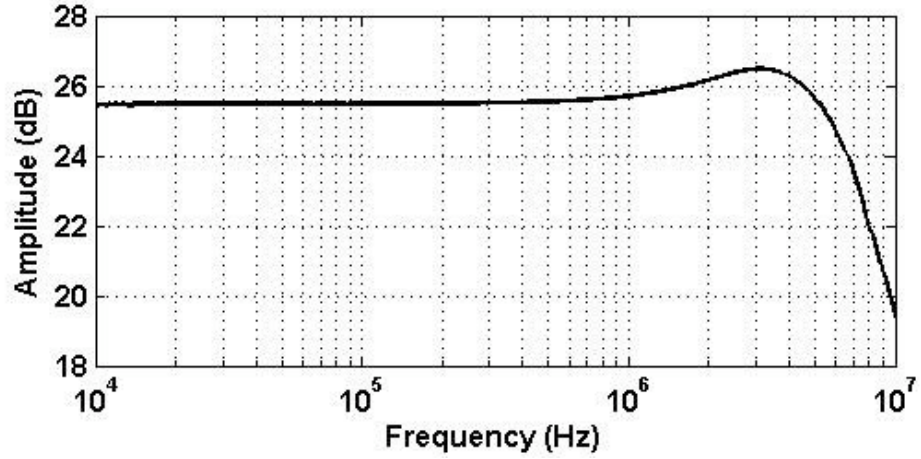

Fig III.5: *Measured amplitude response of the first gain stage.*

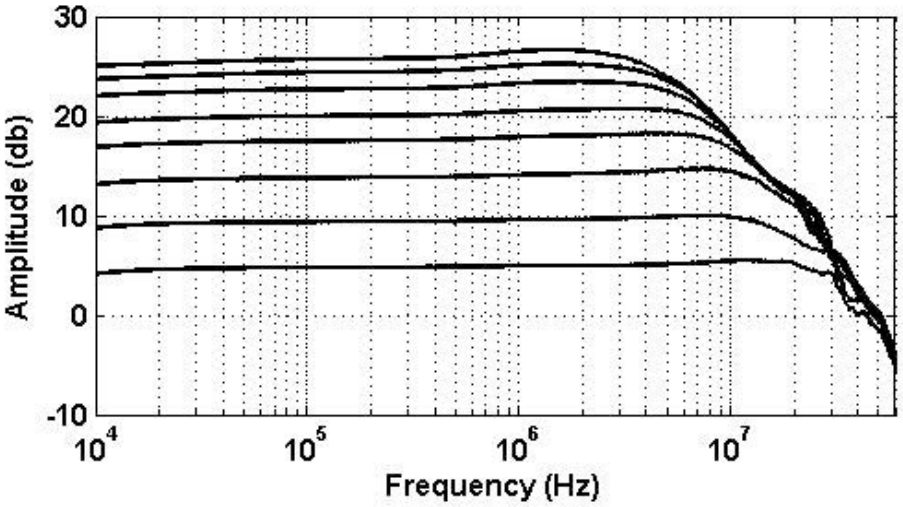

Fig III.6*: Measured closed-loop amplitude response of the second gain stage with HPF connected at its output.*

B. Phase Adjustment

The total phase shift in the entire loop determines the operating point, in other words the oscillation frequency. Unless the phase of the feedback circuitry is exactly the same (with opposite sign) as the phase of the resonator, the oscillation frequency will be different from the resonance frequency. In fact, variations in the phase of the circuitry will cause variations in the oscillation frequency, thus generate frequency noise. The effect of phase variations on oscillation frequency can be reduced by putting the operating point as close as possible to the resonance frequency. Therefore, a phase shifter has to be included in the feedback circuitry to make the phase in the loop close to 0º by overcoming the phase shifts of the resonator and circuit blocks. A first-order all-pass filter is used as the phase shifter as shown in Fig. III.7. The transfer function of this filter with equal feedback resistors is given by

$$T(j\omega) = -\frac{1 - R_{ph}C_{ph}}{1 + R_{ph}C_{ph}}, \quad |T(j\omega)| = 1, \tag{III.2}$$

$$\theta(j\omega) = -2\arctan(\omega R_{ph}C_{ph}) \,. \tag{III.3}$$

As can be observed from Eq. (III.2) and (III.3), the phase of the input signal can be altered by varying R_{ph} and C_{ph} at different frequencies without changing its amplitude. In this work, R_{ph} and C_{ph} are connected externally, which prevents discrete phase tuning that would occur with on-chip capacitors and resistors. The measured phase response of the phase shifter is shown in Fig. III.8.

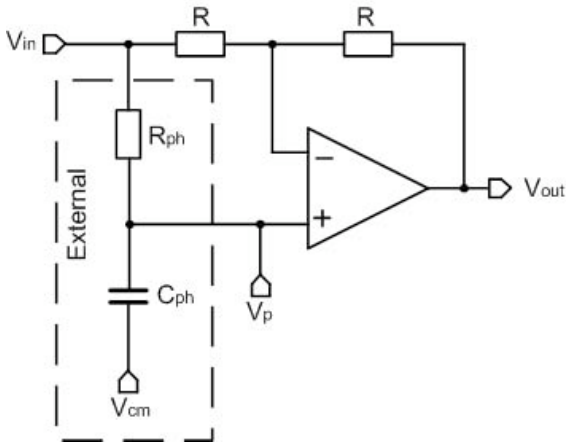

Fig III.7*: Schematic diagram of the phase shifter.*

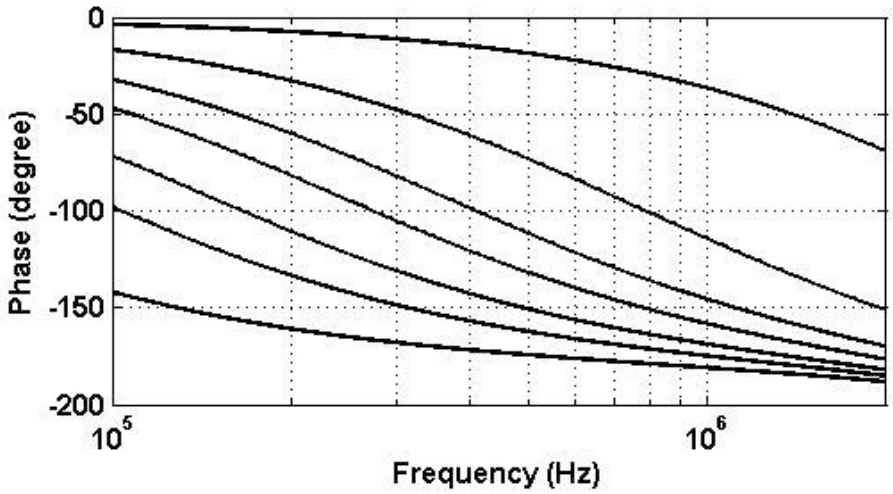

Fig III.8: *Measured phase response of the phase shifter.*

C. Amplitude Limiter

An amplitude limiter is implemented after the phase shifter to prevent the oscillation amplitude from increasing to levels that could saturate the amplifiers, resulting in distortion. The amplitude limiter also converts the sinusoidal oscillation signal into a square wave, which can be directly interfaced to a frequency counter to measure the oscillation frequency.

Fig. III.9 shows the schematic diagram of the amplitude limiter, which is a comparator with hysteresis. With a 40 mV threshold voltage, the hysteresis makes the limiter insensitive to noise and offset. The amplitude limiting is achieved by connecting the supply voltages of an inverter (inv2 in Fig. III.9) and a buffer (buf in Fig. III.9) to desired voltage limits (Vhigh and Vlow). These voltage limits are controllable externally. The outputs out1 and out2 are out-of-phase AC excitation signals.

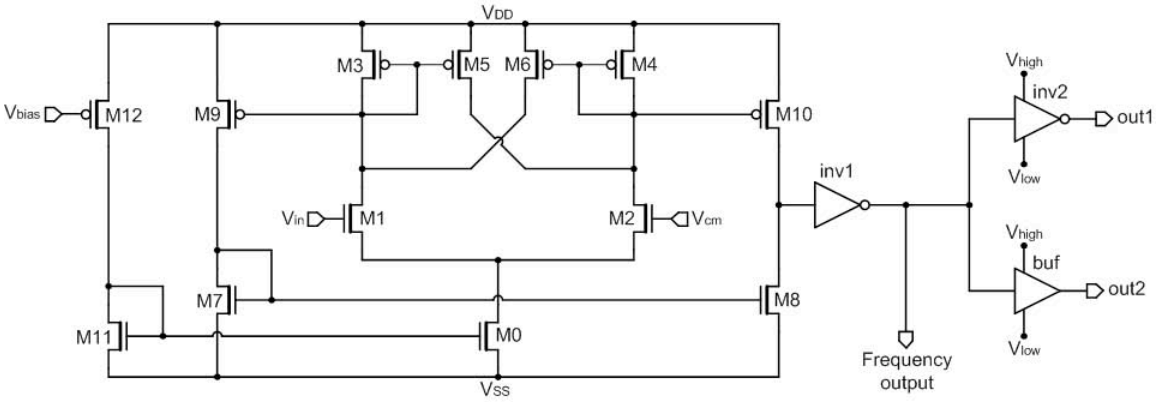

Fig III.9: *Schematic diagram of the amplitude limiter.*

D. Summing Amplifier

To actuate the resonator at its fundamental resonance frequency, a DC-offset has to be added to the amplitude-limited AC excitation signals. Otherwise, all excitation power will be located at DC and twice the resonance frequency. A summing amplifier is used to add this DC-offset. Fig. III.10 shows the schematic diagram and measured amplitude response of the summing amplifier when Voffset is zero.

In the cases where the attenuation from the resonator is high, the excitation signal amplitude and DC-offset have to be large enough to sustain oscillations. Furthermore, the excitation signals have to be buffered to provide sufficient current to the low-resistance excitation resistors without increasing quiescent power consumption. Therefore, an opamp that has a high input voltage range and a high driving capability is needed. A class-AB rail-to-rail input / output opamp meeting these requirements is implemented and used in the summing amplifier (see Fig. III.11).

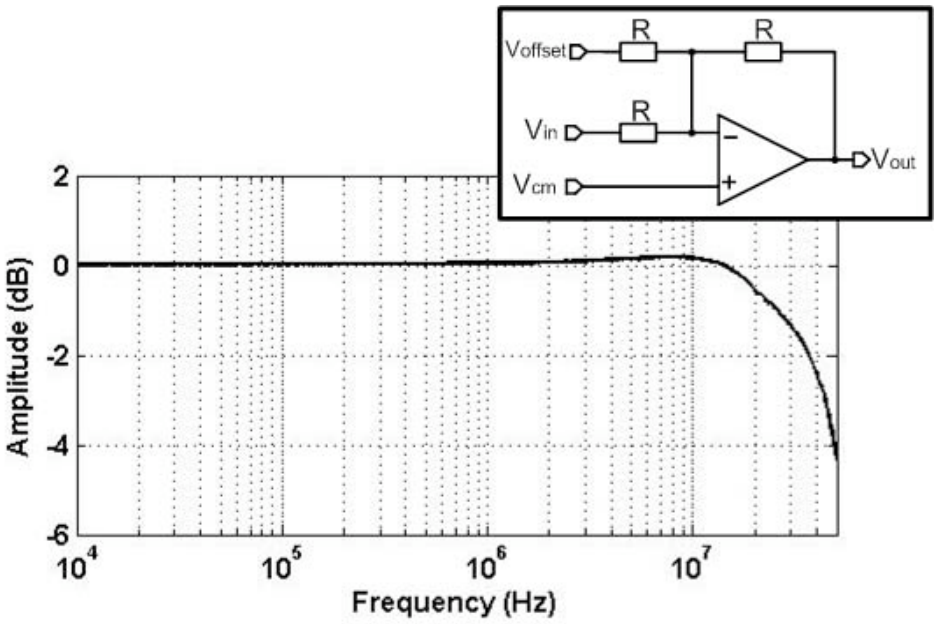

Fig III.10: *Schematic diagram and measured amplitude response of summing amplifier when Voffset is zero.*

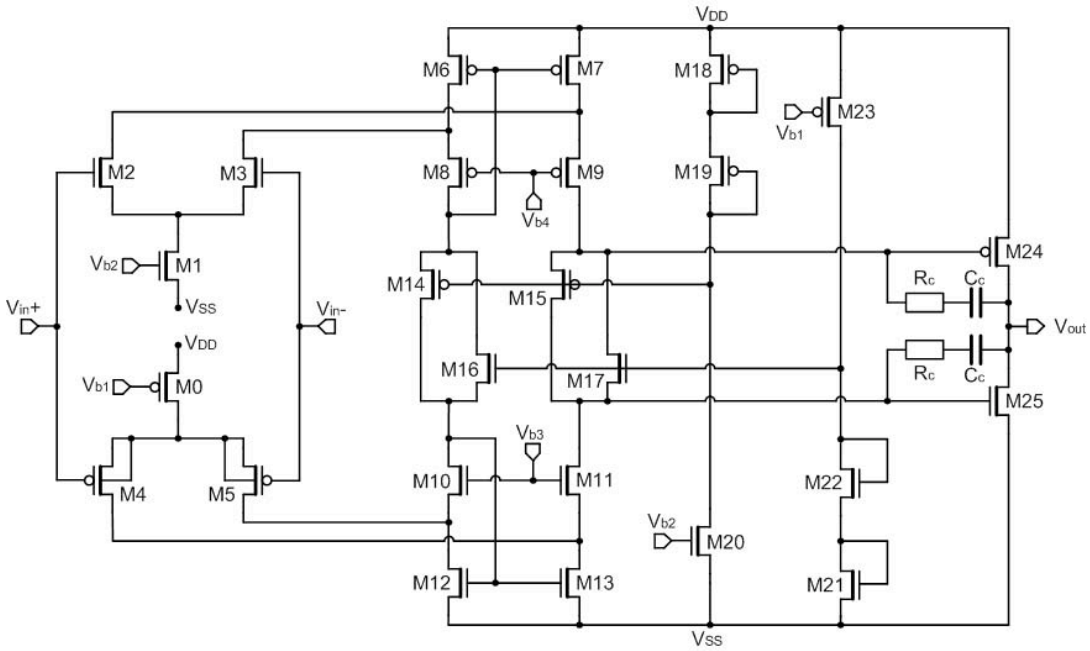

Fig III.11: *Schematic diagram of class AB rail-to-rail input / output opamp.*

IV. Drift Compensation Techniques

The resonance frequency of a microstructure is affected by mass or stiffness changes of the resonator. The relative resonance frequency change of a resonator is given by Eqn I.3. If the resonator is applied as a mass sensitive sensor, the stiffness change (second term in Eqn I.3) is generally assumed to be negligible compared to the mass change. However, if

the mass loading of the resonant microstructure is small, the resonance frequency change induced by a stiffness change should not be neglected anymore.

Fig IV.1 shows the Allan variances as a function of the gate time when the mass of the resonant sensor is constant. The increase in Allan variance with gate time, meaning a decreasing frequency stability, is caused by the drift of the resonance frequency. This drift is mainly due to the change in stiffness. Therefore, without compensating for the frequency change caused by a stiffness change, a high mass resolution cannot be achieved.

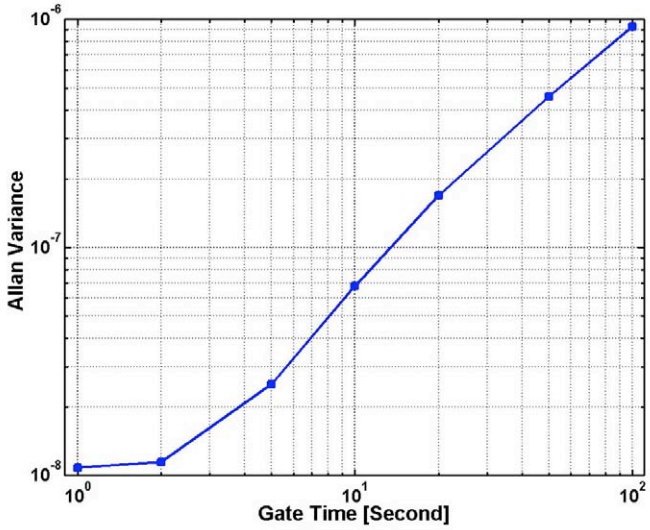

Fig IV.1: *Allan variances of disk resonator as a function of gate time.*

The origins of the frequency drift include environmental parameter changes, such as temperature and humidity, as well as microstructure aging. Most of these effects ultimately change the resonator's spring constant and must be compensated for in order to ensure high sensor resolution. Typically, temperature is the most important environmental parameter and many compensation approaches focus on temperature compensation. Few approaches target compensation of other environmental parameters, such as humidity, or allow for closed-loop operation of the resonant sensor. In the following, we will briefly highlight two techniques, which have been specifically developed for mass-sensitive sensors to compensate for changes in the spring constant of the microresonators. As can be seen from Eq. I.3, a high mass-resolution can only be achieved if the spring constant does not change over time or any spring constant changes are compensated for.

IV.1. Compensation by Stiffness Modulation

The first approach is based on a controlled stiffness modulation of the microsystem using a second feedback loop (see Fig. IV.2). Depending on whether a linear amplifier (switch in position (a) in Fig. IV.2) or an amplitude-limiting comparator (switch in position (b) in

Fig. IV.2) is used in the modulation loop, either relative spring constant changes or quality factor changes of the microresonator can be extracted from the ratio of the resonance frequencies with and without enabled modulation loop.

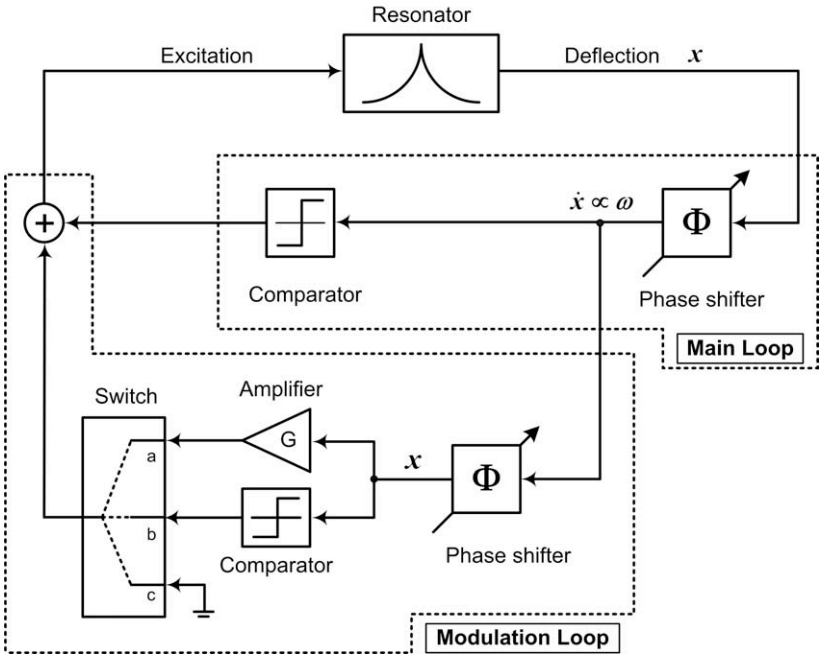

Fig IV.2: *Schematic diagram of feedback circuitry with main loop and modulation loop for spring constant and Q-factor tracking.*

Fig. IV.3 shows the resonance frequency of a disk-type resonator over time, with the modulation loop enabled every 52 s. By extracting the Q-factor from the frequency data and using an initial calibration step to record the temperature dependence of the Q-factor, a temperature compensation of the resonance frequency can be performed in closed-loop operation, improving the temperature coefficient of the resonator from 33 to less than 2 ppm/˚C.

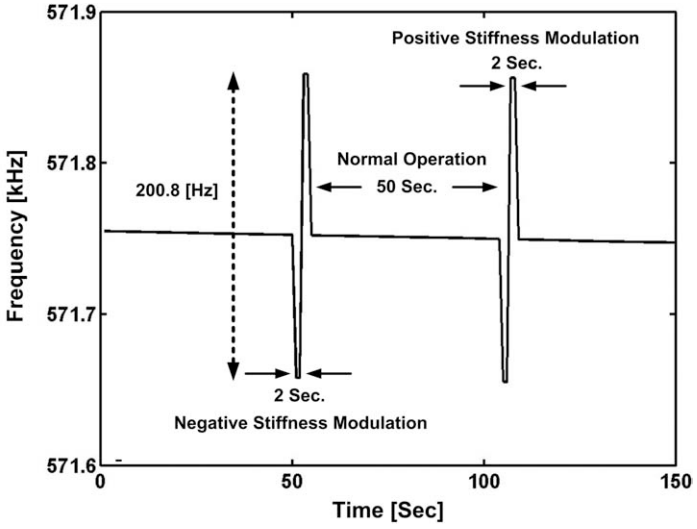

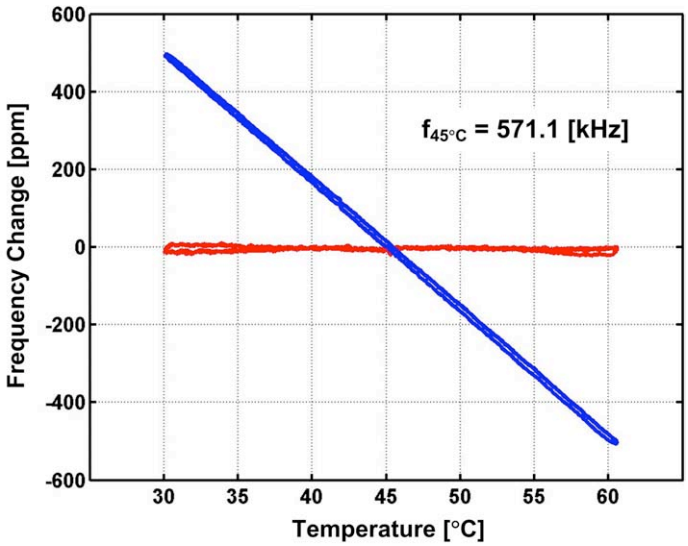

Fig IV.3: *(a) Resonance frequency of disk-type resonator with periodically enabled positive/negative stiffness modulation; (b) Relative resonance frequency change of disk-type microresonator as a function of temperature without temperature compensation (blue line) and with temperature compensation based on the Q-factor (red line); the reference frequency is 571.1 kHz at 45˚C.*

IV.2. Compensation by Resonance Mode and Effective Mass

The second approach utilizes the fact that the resonance frequencies of the flexural modes of e.g. prismatic, homogeneous beams are only different by a well-defined coefficient λ_i:

$$f_i = \frac{\lambda_i^2}{2\pi\sqrt{12}} \frac{t}{L^2} \sqrt{\frac{\hat{E}}{\rho}} \qquad \text{(IV.1)}$$

Here, t, L, $\hat{E}$ and ρ denote the cantilever thickness, length, effective Young's modulus and density, respectively. If such a prismatic beam is used as a mass-sensitive sensor and only *partly covered* along its length with the sensing film, e.g. a chemically sensitive polymer layer, the relative frequency difference of two flexural modes $\Delta f_i / f_i - \Delta f_j / f_j$ depends on the absorbed mass, but not on environmental parameter changes, such as temperature or humidity. A condition for this approach is that the added mass only contributes to the effective mass of the cantilever but not its spring constant.

Fig. IV.4 summarizes the experimental verification of this compensation method using a silicon cantilever that is loaded with a stripe of photoresist. While the relative frequency change of individual flexural modes exhibits a typical temperature coefficient of approx. – 20 ppm/˚C, the relative frequency difference of the second and third mode shows a temperature coefficient of only 0.2 ppm/˚C. The reason that the frequency difference is still dependent on the added mass stems from the fact that the effective mass is different for each flexural mode in case of a partly covered cantilever.

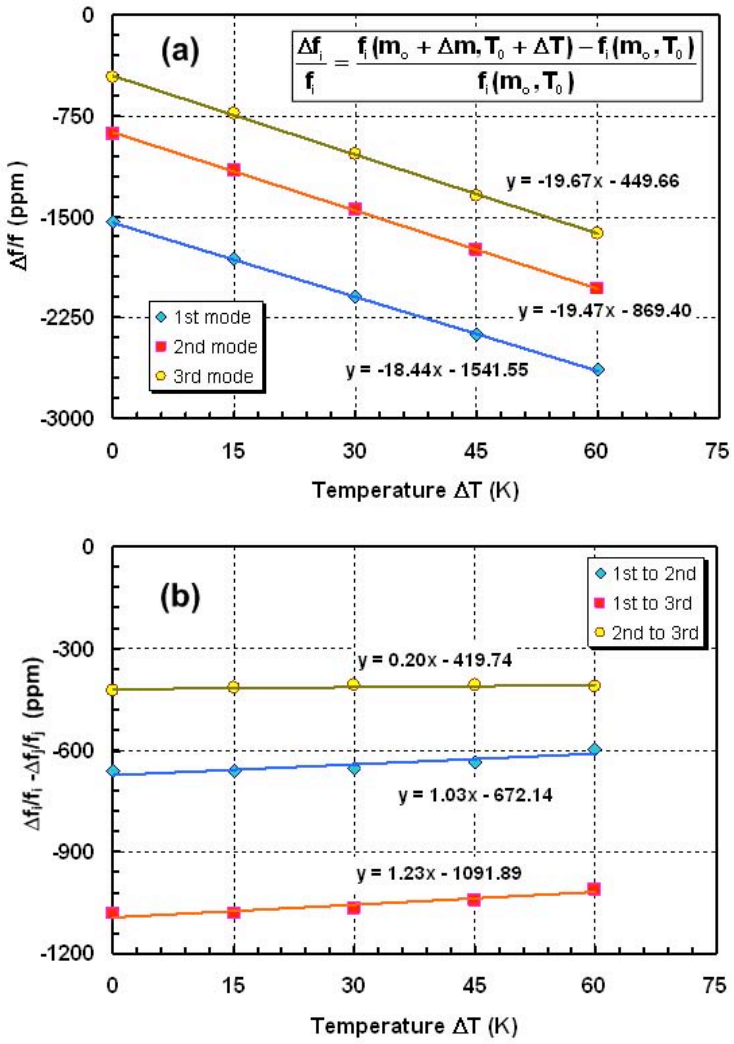

Fig IV.4: *Relative frequency shift of first three flexural modes of silicon cantilever subject to mass loading by photoresist strip as a function of temperature; (b) Difference of relative frequency changes of flexural resonance modes as a function of temperature.*

V. Chemical Measurements

This section of the project focuses on the detection of volatile organic compounds in air using the fabricated disk-shape resonators. Responsive sensing layers are a vital component of chemical sensor systems, providing selective analyte enrichment and recognition at the sensor surface. Thin films of polymers enable diffusion-controlled recognition of gaseous molecules at the sensor surface, giving rise to mass changes detected with high sensitivity by the proposed high-Q resonators.

V.1. Surface Functionalization

The polymers selected as sensitive layers should maintain good adhesion to the resonator surface enabling stable and reliable operation of the sensor system, i.e. the polymer should not peel off during operation. Spray-coating of the polymers offers an easy solution while providing good adhesion.

The resonator semi-disks were spray-coated with either PIB or PECH as a chemically sensitive polymer film. The PIB and PECH polymers used in this research were dissolved in toluene (J.T. Baker HPLC grade) using agitators. The polymer solutions were subsequently sprayed onto the resonators using a calibrated spray gun setup, and then exposed to a toluene vapor environment to achieve better uniformity. The spray gun setup was cleaned using toluene. The deposited film thickness was measured using a profilometer.

V.2. Measurement Setups

Chemical measurements in air were conducted either using a computer-controlled gas mixing system or an exponential dilution chamber. The *gas mixing system* consists of a supply of synthetic air as a carrier gas, which is passed through thermostated bubblers containing a quartz sand matrix soaked with analyte. Using mass flow controlled gas lines, the analyte loaded carrier gas can be further diluted with synthetic air. The resulting analyte/air mixture is then drafted onto the resonator in an air-tight chamber. The resonator die is mounted in a 28-pin dual in-line (DIL) package and wire bonded. The resonant frequency change of the resonator was recorded using a frequency counter connected to the off- chip feedback loop circuitry. All analyte/carrier gas mixtures were brought to 30 °C before being exposed to the resonator. The total gas flow for the reported experiments was 200 sccm. A diagram of the gas-mixing system is shown in Fig. V.1.

In case of the *exponential dilution chamber*, a known volume of analyte is injected into a chamber with known volume and continuously diluted by nitrogen flowing through the chamber at a constant rate of 30 ml/min. The time-dependent analyte concentration in the measurement chamber is given by Eq. (V.1), where C_o is the initial analyte concentration inside the dilution chamber and α is the ratio of the nitrogen flow rate to the dilution chamber volume. The diluted analyte is drafted onto the resonator.

$$C_{analyte} = C_o e^{-\alpha t} \qquad \textbf{(V.I)}$$

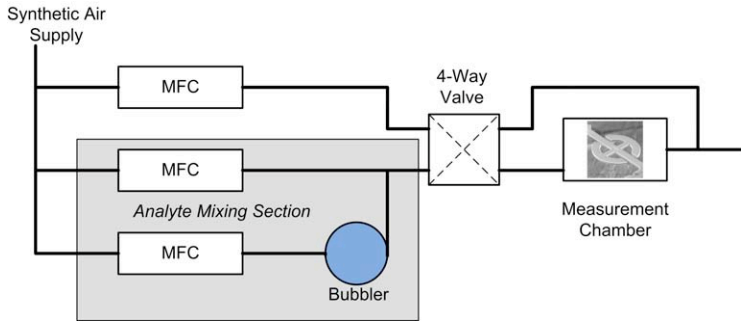

Fig V.1: *Diagram of gas-mixing system: synthetic air is fed to an analyte bubbler to create a gas-vapor mixture, which is further mixed with synthetic air to control the analyte concentration. A 4-way valve alternates the measurement chamber flow between pure synthetic air and the analyte-vapor mixture. Digital mass flow controllers are used to ensure stable analyte concentrations..*

V.3. Chemical Data: Sensitivity and Resolution

Chemical Measurements with Disk-Type Microresonators

Using a gas mixing setup at ETH Zurich, Switzerland, results were obtained for a variety of VOCs in the gas phase using PIB and PECH sensitive layers. A composite of two separate gas measurements is shown in Fig. V.2, exposing two resonators with 4 µm PIB and PECH coatings to different concentrations of o-xylene. The sensors show a response to the analyte injection within a few seconds.

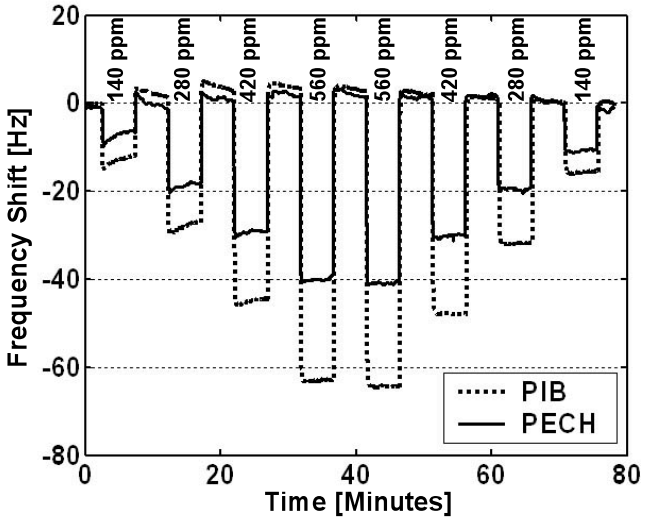

Fig V.2: *Resonance frequency shifts of sensors with PIB and PECH coatings upon exposure to different concentrations of o-xylene in the gas phase. The PIB and PECH thickness is 4 µm.*

The resulting sensor sensitivities shown in Fig. V.3 for given analyte/polymer combinations are largely determined by the sorption behavior of the analyte in the

polymer, as expressed by the partition coefficient of a given analyte/polymer pair, the mass sensitivity of the resonator, and the volume/mass of the deposited sensing film. The partitioning of analytes between the polymer and ambient depends on the dynamic operation mode of the sensor. However, generally higher partition coefficients are found for toluene and benzene in PECH than in PIB. This can be due to a thinner PECH film, which is confirmed by the smaller post-coating frequency change of the PECH coated resonator (20 kHz vs. 25 kHz).

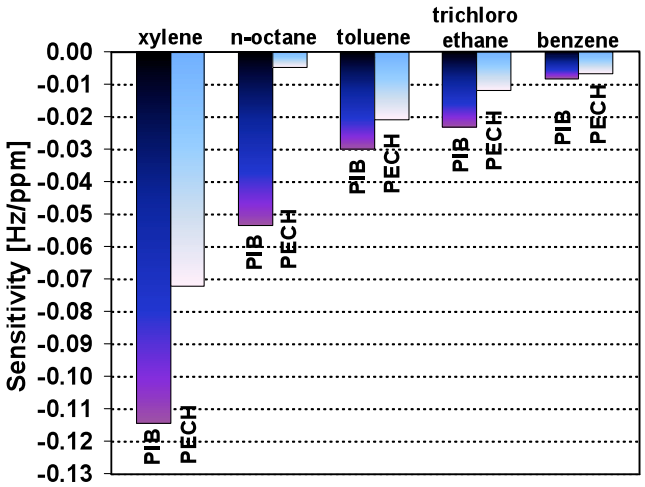

Fig V.3: *Sensitivities of PIB and PECH coated resonators for different VOCs in the gas phase.*

Limits of detection were calculated from the sensitivity data, assuming the minimum detectable frequency change to be 3 times the noise level determined by the Allan variance method. Consequently, o-xylene has a gas phase limit of detection of 2.2 ppm in these experiments.

Comparison of Disk- and Annular-Type Resonators

In a second set of experiments carried out at ETH Zurich, Switzerland (as part of an IREE supplement), different disk- and annular-type microresonators were compared in terms of their chemical sensitivity and resolution. The sensors were individually spray-coated with a 1% (w/v) solution of highly cross-linked PIB and toluene. The thicknesses of the polymer coatings (≤ 100 nm) were confirmed with profilometer measurements of samples coated alongside the working devices. The resonators were operated in an amplifying feedback loop, which continuously excites the resonator in its in-plane mode. The added mass related to analyte adsorption results in a frequency decrease, which was tracked by a frequency counter. Annular- and disk-type resonators (see Fig. I.5) with outer radii of 150 and 200 µm were exposed to different toluene concentrations in the gas-mixing system, with intermittent exposures to pure synthetic air as a reference gas. As an example, Fig. V.4 shows the transient response of an annular resonator with outer radius of 150µm to different toluene concentrations.

From the frequency data, the sensor sensitivity and the short-term frequency stability are

extracted and the sensor limit of detection (LOD) is calculated as three times the noise-equivalent analyte concentration c_{min} (see Table V.1). Fig. V.5 summarizes the sensor LOD for toluene as a function of the outer radius, showing that the annular design generally outperforms the disk design even though the disk design exhibits larger polymer areas. Moreover, thinner sensors offer better resolution for a given polymer film thickness. As a result, the best LOD of 18.3 ppm was achieved by a 5 µm thick annular design with 150 µm outer radius, even though it was covered with only a 20 nm PIB film. Increasing the film thickness will further lower this LOD.

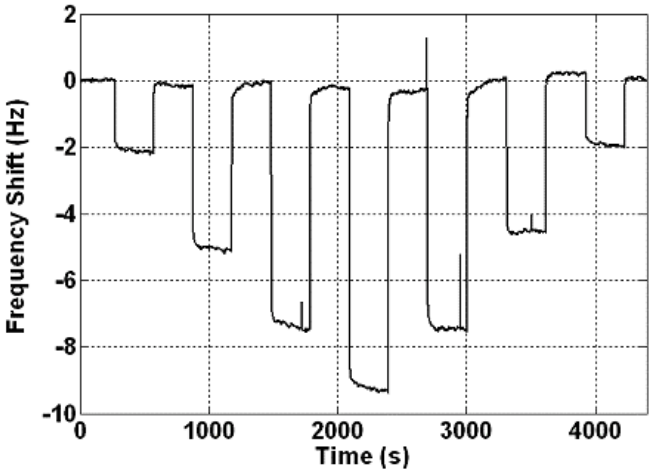

Fig V.4: *Frequency shift vs. time for a 25 µm thick annular resonator upon exposure to different concentrations of toluene.*

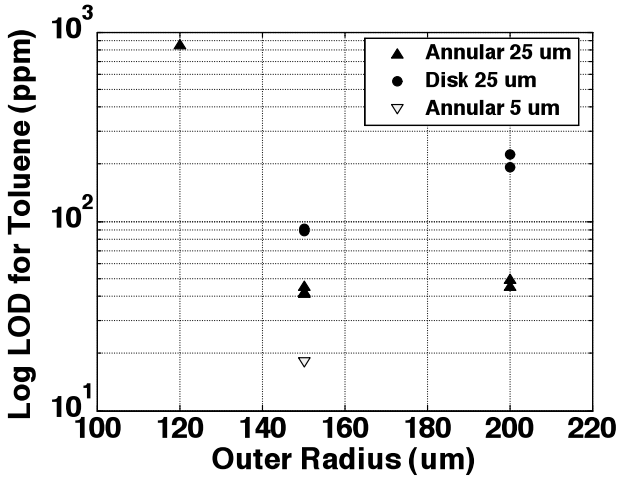

Fig V.5: *Toluene LODs of annular and disk resonators with 5 and 25 µm thicknesses as a function of the outer radius. PIB coatings are between 20 and 85nm thick.*

Table V.1. *Toluene sensitivity and resolution of disk and annular devices with different dimensions; the PIB film thicknesses range from 20-85nm, affecting sensitivity and resolution.*

Device Type	Device Thickness (µm)	PIB Coating Thickness (nm)	Outer Radius (µm)	Resolution (ppm)	Sensitivity (Hz/ppm)
Disk	25	66.5	150	89	1.28×10^{-3}
Disk	25	66.5	200	194	8.78×10^{-4}
Annular	5	20.0	150	18.3	1.01×10^{-3}
Annular	25	85.0	120	844	7.58×10^{-4}
Annular	25	75.0	150	41.5	1.74×10^{-3}
Annular	25	69.5	200	44.7	1.17×10^{-4}

The experimentally obtained sensitivities for the disk and annular devices agree well with FEM simulations. Fig. V.6(a) shows simulated sensitivities for disk and annular device types of 25 and 5 µm thicknesses, assuming a 1 µm PIB layer. The deviations in the experimental results from the simulated results are attributed mainly to variations in the resonator and polymer thickness. It is worth noting that the sensor sensitivity normalized by the resonance frequency (Fig. V.6(b)) is almost independent of the lateral device geometry for uniformly coated in-plane resonators, and increases with decreasing device thickness. The improved sensitivity of the thinner devices is, however, at least partly offset by their reduced short-term frequency stability.

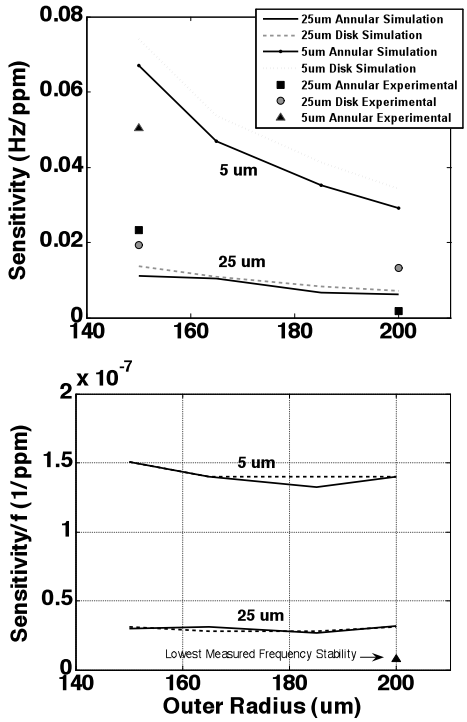

Fig V.6: *Simulated (a) sensor sensitivity to toluene and (b) sensor sensitivity normalized to the in-plane resonance frequency as a function of the device outer radius assuming a PIB thicknesses of 1um. The symbols correspond to experimental data (see Table V.1) scaled to a polymer thickness of 1 µm for comparison.*

The normalized sensor sensitivities displayed in Figure V.6(b) can be directly compared with the Allan variance metric used to measure frequency stability. Considering that Alan variances as low as 7.8×10^{-9} were achieved for polymer-coated annular resonators, sub-ppm LODs should be feasible with increased polymer thicknesses on the order of 1 μm.

V.4. Chemical Measurement with CMOS Interface Circuitry

In the interfacing experiments, a resonator with resonance frequency of approximately 427.2 kHz was spray-coated with polyisobutylene (PIB) as the chemically sensitive polymer film and interfaced with the CMOS chip through hybrid connections. Fig. V.7 shows the closed-loop oscillation and excitation signals and the spectrum of the signal after first gain stage.

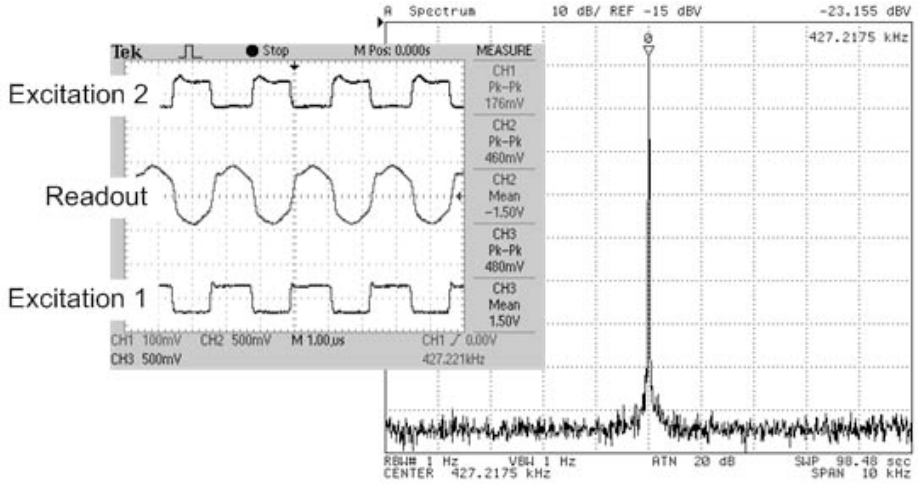

Fig V.7: *Closed-loop oscillation and excitation signals and the spectrum after the first gain stage.*

Gas-phase chemical measurements have been carried out using the exponential dilution setup. The resonator was placed in an air-tight measurement chamber. A known volume of toluene was injected into the exponential dilution chamber and continuously diluted. The diluted analyte was drafted onto the resonator. Fig. V.8 shows the frequency shift upon exposure to different concentrations of toluene in the gas-phase and the recorded frequency change with a gate time of 1 second (inset). The Allan variance of the spray-coated microsensor mounted in the measurement chamber was determined to be 3.76×10^{-8}, corresponding to a short-term frequency stability of 16 mHz. The limit of detection (LOD) of the sensor system is found to be 13 ppm for toluene.

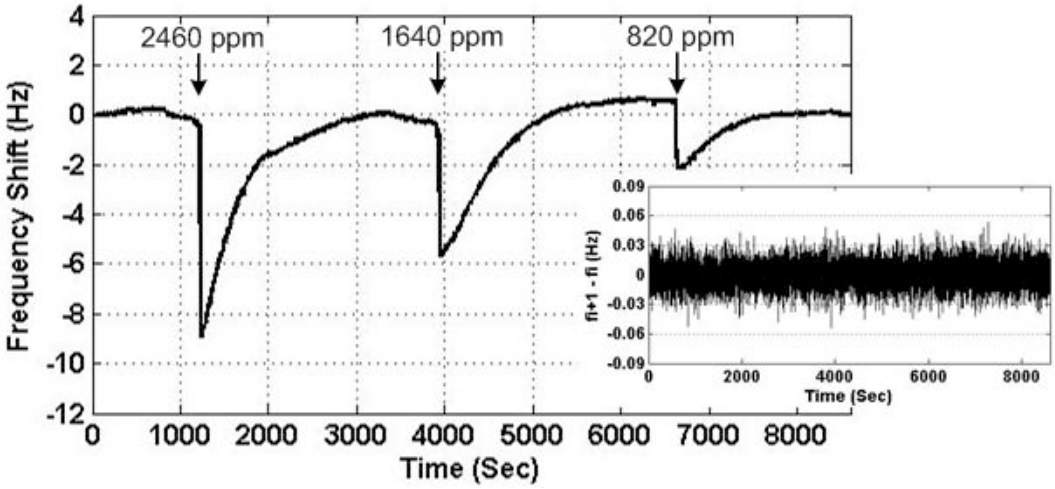

Fig V.8: *Frequency shift upon exposure to different concentrations of toluene and the recorded frequency change with a gate time of 1 second (inset).*

V.5. Chemical Measurement with Drift Compensation

For the application as a mass-sensitive sensor, the microresonator is generally incorporated in an amplifying feedback loop as the frequency-determining element. In this feedback loop (see main loop in Fig. V.9), the resonator output signal is amplified and phase matched with the vibration velocity of the resonator; the resulting signal is amplitude-limited using a comparator and fed back to the excitation terminal via a buffer amplifier. This primary excitation signal compensates for the resonator damping and a constant-amplitude oscillation is sustained at the mechanical resonance frequency. This way, the measurand induced frequency change can be simply detected by using a frequency counter.

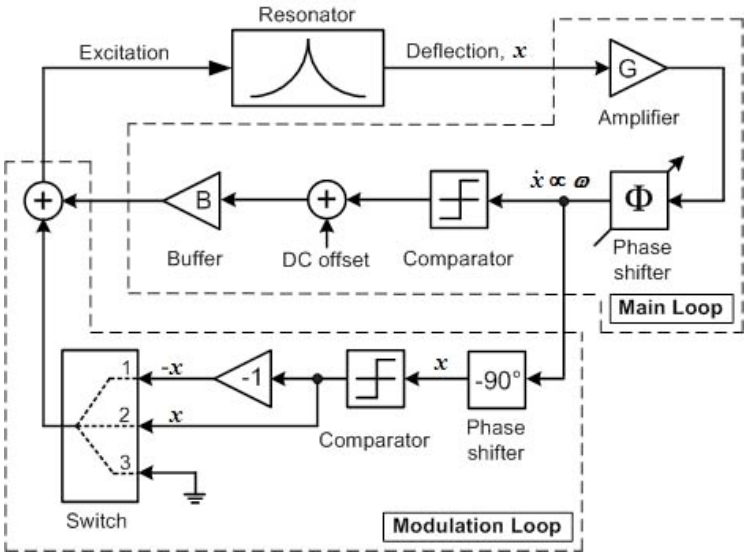

Fig V.9: *Schematic diagram of feedback circuitry for resonator with main loop and modulation loop for the implemented drift compensation method.*

Besides the main loop, a second electronic feedback loop generates a signal in-phase with the deflection of the resonator (see modulation loop in Fig. V.9 and Section IV.1). This signal is applied to the resonator excitation elements in addition to the signal generated by the main loop and modulates the effective stiffness of the resonator. By controlling the polarity of the modulation signal, the effective stiffness of the resonator can be either reduced or increased. As a result, the resonance frequency of the harmonic oscillator is changed in response to the modulated effective stiffness.

The force-deflection relation of a mechanical resonator when modeled by a simple second-order system consisting of mass m, damper b and spring k is given by Eq. (V.2). The motion of the resonator considered in this work with main loop and enabled modulation loop can be described by Eq. (V.3) using the describing function of a comparator, defined as the complex ratio of the fundamental harmonic component of the comparator output signal to its input sinusoidal signal.

$$m\ddot{x} + b\dot{x} + kx = F \qquad \textbf{(V.2)}$$

$$m\ddot{x} + b\dot{x} + kx = \psi_{main}\frac{\dot{x}}{|\dot{x}|} \mp \psi_{\mathrm{mod}}\frac{x}{|x|} \qquad \textbf{(V.3)}$$

The force amplitudes ψ_{main} and ψ_{mod} in Eq. (V.3) are defined as

$$\psi_{main} = \chi\gamma\frac{4M_{main}}{\pi}, \quad \psi_{\mathrm{mod}} = \chi\gamma\frac{4M_{\mathrm{mod}}}{\pi} \qquad \textbf{(V.4)}$$

Here, χ is the transfer function of the generated mechanical force to an applied electrical excitation signal, γ is the transfer function of the electrical read-out signal to the resonator deflection, and M_{main} and M_{mod} are the amplitudes of the square wave signals generated by the comparators in the main and modulation loop, respectively. Combining Eqs. (V.3) and (V.4), the system equation for the resonator shown in Fig. V.9 is expressed by

$$m\ddot{x} + \left[b - \frac{\psi_{main}}{|\dot{x}|}\right]\dot{x} + \left[k \pm \frac{\psi_{\mathrm{mod}}}{|x|}\right]x = 0 \qquad \textbf{(V.5)}$$

Under steady-state oscillation, the force generated by the main loop is the same as the damping force of the resonator. In this case, the magnitudes of the steady-state vibration velocity $\dot{x}$ and the vibration amplitude x of the resonator embedded in the feedback circuit are obtained from Eq. (V.5) by forcing the effective damping force (second term in Eq. (V.5)) to zero, i.e.

$$\dot{x} = \frac{\psi_{main}}{b}, x = \frac{\psi_{main}}{b\omega_o} \qquad \textbf{(V.6)}$$

As a result, the equation of motion becomes:

$$m\ddot{x} + \left[k \pm \frac{\psi_{\mathrm{mod}}}{\psi_{main}} b\omega_o \right] x = 0 \qquad \textbf{(V.7)}$$

Using the relation $Q = k\, b^{-1}\, \omega_0^{-1}$, Eq. (V.7) can be expressed in terms of Q-factor by

$$m\ddot{x} + \left[k\left(1 \pm \frac{\psi_{\mathrm{mod}}}{\psi_{main}} \frac{1}{Q} \right) \right] x = 0 \qquad \textbf{(V.8)}$$

Eq. (V.8) can be simplified to Eq. (V.9), if the amplitudes of the excitation signals generated by the main and modulation loops are equal, i.e. $\psi_{main} = \psi_{mod}$

$$m\ddot{x} + \left[k\left(1 \pm \frac{1}{Q} \right) \right] x = 0 \qquad \textbf{(V.9)}$$

Eq. (V.9) reveals that the relative stiffness change induced by the modulation loop is directly related to the Q-factor of the resonator. In fact, the stiffness is modified by a factor of $(1 \pm Q^{-1})$ by the modulation loop in Fig. V.9.

It should be noted that Eqs. (V.3) - (V.9) only hold when the excitation signals generated by main and modulation loop are exactly phase matched with the vibration velocity $\dot{x}$ and the deflection of the resonator x, respectively. In a real system, the phase-tuning is done by an electronic circuit, such as an all-pass filter, and there is a possibility of a tuning error, which will introduce an error in the estimated Q-factor. To minimize this phase tuning error, the polarity of the signal generated by the modulation loop is altered to obtain both positive and negative stiffness modulations, resulting in an increase or decrease in the resonance frequency. In this case, the resonance frequencies with positive and negative stiffness modulation, respectively, become

$$\omega_{pos} = \sqrt{\frac{k(1+1/Q)}{m}}, \quad \omega_{neg} = \sqrt{\frac{k(1-1/Q)}{m}} \qquad \textbf{(V.10)}$$

From the ratio of the frequencies $\omega_{pos}/\omega_{neg}$, the Q-factor of the resonator can be calculated as

$$Q = \frac{\alpha+1}{\alpha-1}, \quad \alpha = \left(\frac{\omega_{pos}}{\omega_{neg}} \right)^2 \qquad \textbf{(V.11)}$$

Therefore, by measuring the resonance frequency changes caused by the periodically enabled modulation loop of Fig. V.9, the Q-factor (or the relative Q-factor change) of a microresonator can be extracted and tracked during closed-loop sensor operation.

If the influence of the Q-factor on the resonance frequency is known, the measured Q-factor data can be used to compensate for frequency drift. In the present work, an initial calibration step establishes the relation between the relative Q-factor dQ/Q and frequency $d\omega_0/\omega_0$ changes. A custom-made printed circuit board includes the feedback circuitry shown in Fig. V.9. A LabView program controls the switch position shown in Fig. V.9

via a National Instruments data acquisition (DAQ) card and reads the resonance frequency from a frequency counter.

The measurements have been performed with a silicon-based disk-type microresonator and the microresonator was spray-coated with polyisobutylene (PIB) as chemically sensitive polymer film. The film thickness was measured as 0.3μm using a profilometer. Thereafter, the resonator is placed inside the air-tight measurement chamber and analyte-loaded gas streams are generated with an exponential dilution chamber.

During the chemical measurements, the negative and positive stiffness modulation (switch position 1 and 2 in Fig. V.9) are periodically enabled for 2 seconds each, every 54 seconds (see Fig. V.10). The disk-type resonator with a 533.4 kHz resonance frequency showed a frequency change (f_{pos} - f_{neg}) of approximately 241 Hz by the enabled modulation loop. Generally, a larger Q-factor yields a smaller frequency change (f_{pos} - f_{neg}). To prevent variations in resonance frequency by different static power dissipations in the excitation resistors with enabled and disabled modulation loop, the static power dissipation produced by the electrothermal excitation elements is kept constant during the experiment.

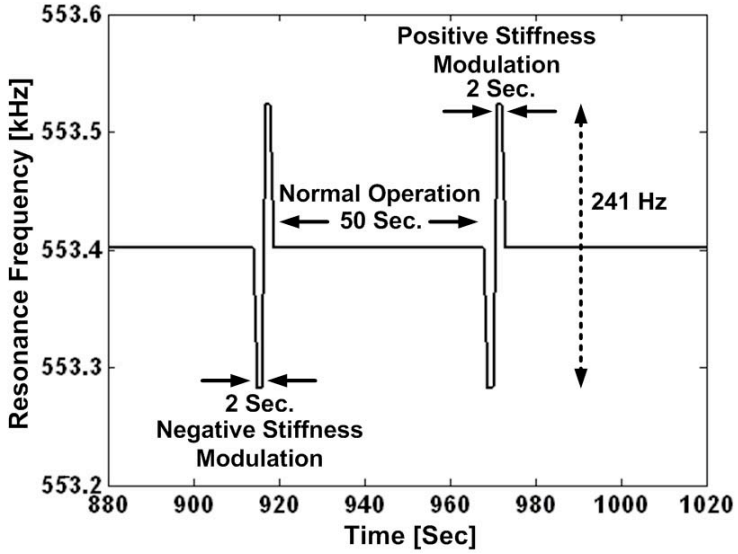

Fig V.10: *Resonance frequency of disk-type resonator with periodically enabled positive and negative stiffness modulation.*

Fig. V.11 shows the resonance frequency change with and without compensation during a gas-phase chemical measurement without temperature control, with two subsequent analyte injections into the exponential dilution chamber with different ethyl chloride concentrations. The Q-factor is extracted using Eq. (V.11) and shown in Fig. V.12. Using this extracted Q-factor, the frequency change stemming from the Q-factor change is estimated using the relation $dQ/Q = 360\ d\omega_0/\omega_0$ obtained in the initial calibration step. This estimated frequency change is shown as the dotted line in Fig. V.11 and is used to compensate for frequency drift. The final compensated frequency signal (dashed line in

Fig. V.11) is simply the difference of the measured (solid line) and estimated frequency (dotted line). In the measurement shown in Fig. V.11, the observed frequency drift of 15Hz is caused by a roughly 1˚C temperature decrease during the entire measurement. After compensation, the frequency is stable to within ±0.3Hz over the 2.5 hour measurement time, and the frequency decreases during analyte exposure are clearly visible.

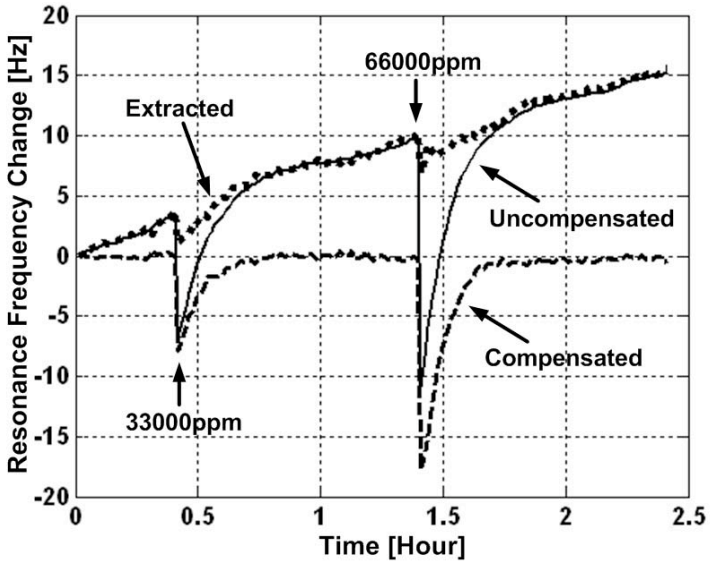

Fig V.11: *Resonance frequency change with (dashed line) and without (solid line) compensation during a gas-phase chemical measurement; the resonator (f=553.4kHz) is subsequently exposed to different concentrations of ethyl chloride. The dotted line shows the extracted frequency change based on the Q-factor measurement.*

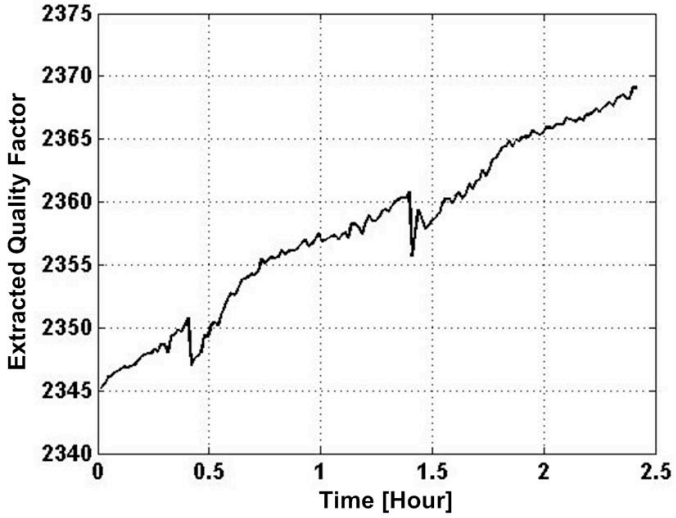

Fig V.12: *Extracted Q-factor from Eq. (10) during the gas-phase chemical measurement shown in Fig. V.11.*

VI. Publications

1. J.H. Seo, K.S. Demirci, A. Byun, S. Truax, O. Brand, "Novel temperature compensation scheme for microresonators based on controlled stiffness modulation," in *Transducers '07*, *Digest of Technical Papers*, 2007, pp. 2457-2460.
2. S. Truax, K.S. Demirci, J.H. Seo, P. Kurzawski, Y. Luzinova, A. Hierlemann, B. Mizaikoff, O. Brand, "Gas and liquid phase sensing of volatile organics with disk microresonator," in *Proc. 2008 IEEE Microelectromechanical Systems Conference* (MEMS 2008), 2008, pp. 220-223.
3. J.H. Seo, K.S. Demirci, S. Truax, L.A. Beardslee, O. Brand, "Tracking microresonator Q-factor in closed-loop operation," in: *Proc. 2008 Solid-State Sensor, Actuator and Microsystem Workshop*, Hilton Head, 2008, pp. 190-193.
4. S. Truax, K.S. Demirci, J.H. Seo, P. Kurzawski, Y. Luzinova, A. Hierlemann, B. Mizaikoff, O. Brand, "Sensing of volatile organics with disk microresonators," *Proc. Eurosensors 2008*, 2008.
5. O. Brand (invited paper), K. Naeli, K.S. Demirci, S. Truax, J.H. Seo, "Silicon-Based Resonant Sensors," in *Proc. Micromechanics Europe Workshop 2008*, Aachen, Germany, 2008, pp. 121-127.
6. J.H. Seo, O. Brand, "High Q-factor in-plane mode resonant microsensor for gaseous/liquid environment," *IEEE J. Microelectromechanical Systems*, vol. 17, pp. 483-493, 2008.
7. J.H. Seo, K.S. Demirci, A. Byun, S. Truax, O. Brand, "Temperature compensation method for resonant microsensors based on a controlled stiffness modulation," *Journal of Applied Physics*, vol. 104, 2008, pp. 014911-1-9.
8. K.S. Demirci, J.H. Seo, S. Truax, L.A. Beardslee, Y. Luzinova, B. Mizaikoff, O. Brand, "Frequency drift compensation in mass-sensitive chemical sensors based on periodic stiffness modulation," in *2009 IEEE Microelectromechanical Systems Conference* (MEMS 2009), 2009, pp. 284-287.
9. S. Truax, K.S. Demirci, A. Hierlemann, O. Brand, "Exploring the resolution of different disk-type chemical sensors," in *Transducers 2009, Digest of Technical Papers*, 2009, pp. 1838-1841
10. K.S. Demirci, S. Truax, L.A. Beardslee, O. Brand, "Chemical Microsystem based on integration of microresonant sensor and CMOS ASIC," in Proc. Custom Integrated Circuit Conference (CICC 2009), 2009, in press.
11. Naeli, O. Brand, "Cancellation of environmental effects in resonant mass sensors based on overtones and effective mass," *Rev. Sci. Instr.*, vol. 80, 2009, pp. 063903-1-8.